Frontiers of Information Technology & Electronic Engineering
www.jzus.zju.edu.cn; engineering.cae.cn; www.springerlink.com
ISSN 2095-9184 (print); ISSN 2095-9230 (online)
E-mail: jzus@zju.edu.cn

An adjustable anti-resonance frequency controller for a dual-stage actuation semi-active vibration isolation system*

Bo ZHAO[1,2], Weijia SHI[†‡1,2], Bingquan WANG[1,2], Jiubin TAN[1,2]

[1]*Center of Ultra-precision Optoelectronic Instrument Engineering, Harbin Institute of Technology, Harbin 150080, China*

[2]*Key Lab of Ultra-precision Intelligent Instrumentation (Harbin Institute of Technology), Ministry of Industry and Information Technology, Harbin 150080, China*

[†]E-mail: shiweijia@hit.edu.cn

Received July 24, 2020; Revision accepted Sept. 18, 2020; Crosschecked May 7, 2021; Published online Aug. 4, 2021

Abstract: In the semiconductor manufacturing industry, the dynamic model of a controlled object is usually obtained from a frequency sweeping method before motion control. However, the existing isolators cannot properly isolate the disturbance of the inertial force on the platform base during frequency sweeping (the frequency is between 0 Hz and the natural frequency). In this paper, an adjustable anti-resonance frequency controller for a dual-stage actuation semi-active vibration isolation system (DSA-SAVIS) is proposed. This system has a significant anti-resonance characteristic; that is, the vibration amplitude can drop to nearly zero at a particular frequency, which is called the anti-resonance frequency. The proposed controller is designed to add an adjustable anti-resonance frequency to fully use this unique anti-resonance characteristic. Experimental results show that the closed-loop transmissibility is less than −15 dB from 0 Hz to the initial anti-resonance frequency. Furthermore, it is less than −30 dB around an added anti-resonance frequency which can be adjusted from 0 Hz to the initial anti-resonance frequency by changing the parameters of the proposed controller. With the proposed controller, the disturbance amplitude of the payload decays from 4 to 0.5 mm/s with a reduction of 87.5% for the impulse disturbance applied to the platform base. Simultaneously, the system can adjust the anti-resonance frequency point in real time by tracking the frequency sweeping disturbances, and a good vibration isolation performance is achieved. This indicates that the DSA-SAVIS and the proposed controller can be applied in the guarantee of an ultra-low vibration environment, especially at frequency sweeping in the semiconductor manufacturing industry.

Key words: Semi-active vibration isolation; Dual-stage actuation; Dynamic vibration absorption; Adjustable anti-resonance frequency controller

https://doi.org/10.1631/FITEE.2000373 **CLC number:** TB53

1 Introduction

It is of great scientific significance and practical value to fully study vibration isolation (Matichard et al., 2015). Vibration isolation is one of the four core technologies of the lithography machine (Ding et al., 2011). Besides, there is an urgent demand for the guarantee of an ultra-low vibration environment in the fields of semiconductor manufacturing (Carre et al., 1982), ultra-precision measurement (Lee et al., 2011; Ito et al., 2015, 2017), ultra-precision processing (Li et al., 2019), floating raft (Zhao and Chen, 2008; Yang et al., 2017), and aerospace (Bronowicki et al., 2003; Butler, 2011; Ismagilov et al., 2020). In the semiconductor manufacturing industry, the dynamic model of a controlled object is usually obtained from a frequency sweeping method before motion control. However, the inertial force generated during frequency sweeping will react with the platform base, which equals the disturbance force that frequency variation exerts on the whole system (Yin et al., 2012).

‡ Corresponding author

* Project supported by the National Natural Science Foundation of China (No. 51975160)

ORCID: Bo ZHAO, https://orcid.org/0000-0003-2859-0180; Weijia SHI, https://orcid.org/0000-0002-3379-0331

Actually, the existing isolators cannot fully isolate the vibration against the perturbation of a specific frequency, especially between 0 Hz and the natural frequency. The proposal of new vibration isolation control methods is necessary to meet similar vibration isolation requirements.

The passive vibration isolation system (PVIS), such as springs, has advantages of simple structure and easy realization (Kamesh et al., 2012; Alujević et al., 2018). However, due to the limitation that the stiffness of springs cannot be infinitely small, PVIS cannot achieve ultra-low frequency vibration isolation (Coronado et al., 2013). Therefore, the active vibration isolation system (AVIS) has been proposed. AVIS is composed of sensors, actuators, a control system, and passive vibration isolation components (Nelson, 1991; Qiu et al., 2018). Compared with PVIS, AVIS can adjust parameters of the system flexibly according to the object of vibration isolation. Therefore, AVIS has advantages of good adaptability, low-frequency vibration isolation, and light weight, and has become the research focus of vibration isolation technology. AVIS is divided into a full-active vibration absorber and a semi-active vibration absorber. Due to the complex structure and the amount of energy consumption of the full-active vibration absorber, the semi-active vibration absorber is more widely applied (Xu JW et al., 2020). Semi-active vibration absorption technology can give suppress vibration isolation by installing a tuned dynamic vibration absorber, which tracks the frequency of the main system vibration by adjusting its natural frequency.

To isolate frequency sweeping disturbances generated during frequency sweeping in the semiconductor industry, variable stiffness technology is the key to determining the vibration isolation performance in the semi-active vibration isolation (Zhang et al., 2019). This technology is divided into mechanical variable stiffness technology (such as the combined beam structure and air spring) and the intelligent material variable stiffness technology (such as piezoelectric materials and shape memory alloys) (Suzuki and Abe, 2013). Brennan (1997) proposed an air spring to design a dynamic absorber that can change the stiffness of the absorber by varying the magnitude of the pressure in the balloon. The air spring is strongly related to the bearing capacity and can be designed at a large size according to the actual needs. In addition, it is durable, has good anti-fatigue properties, and allows a large deformation amount to meet the requirements of low frequency. However, the tuning speed of the air spring dynamic vibration absorber is relatively slow and cannot meet the requirement of higher frequency vibration. Nagaya et al. (1999) proposed an assumption of variable stiffness of a cantilever beam structure, and designed a cantilever beam type semi-active dynamic vibration absorber. However, the longitudinal size of the structure is asymmetrical and large. In addition to applying a vertical force to the damping object, the effect of alternating torque results in the damping object producing unexpected rotation.

Recently, the piezoelectric actuator (PZT) becomes more attractive in the field of vibration isolation because of the advantages of wide band, high precision, fast response, and light weight (Niu JC et al., 2005; Qu et al., 2019; Wang et al., 2019). Davis and Lesieutre (2000) proposed a PZT semi-active dynamic absorber with a frequency shift range of 243–257 Hz using PZT variable stiffness technology. Yong et al. (2004) proposed a method to change the stiffness of the spring and realized the frequency shift of the vibration absorber by controlling the deformation of PZT and adjusting the friction force between PZT and the side wall to change the coupling degree of the two springs. The wide band and large amplitude characteristics of PZT were fully used and the disadvantage of a small deformation of PZT was avoided, but the change in stiffness is not linear and is difficult to control.

In this paper, an adjustable anti-resonance frequency controller for a dual-stage actuation semi-active vibration isolation system (DSA-SAVIS) is proposed and tested to isolate frequency sweeping disturbances instead of using variable stiffness technology. The DSA-SAVIS with the proposed controller has a unique dynamic absorber characteristic and allows an adjusting anti-resonance frequency point in real time by tracking external disturbances. It makes the best of the advantages of both voice coil motor (VCM) and PZT based on the principle of dynamic vibration absorption.

2 Description and mathematical modeling of the system

2.1 Design of the DSA-SAVIS

Based on the analysis of the dynamic vibration absorption principle, the prototype of the DSA-SAVIS is designed (Fig. 1), including the payload, base, connecting plate, air floating rails, passive vibration isolation spring, active actuator VCM, and PZT. The VCM has a long motion stroke with zero stiffness. However, it works only in low frequency band, and its resolution is not high enough for the isolation of micro vibration. The PZT has advantages such as wide band and extremely high resolution, but the stroke of the PZT is only a few tens of microns. The proposed dual-stage actuator (DSA) is created by serially connecting a VCM onto a PZT. The DSA combines their advantages and obtains wide control frequency band, high resolution, and long motion stroke in the SAVIS.

The schematic of the designed DSA-SAVIS is shown in Fig. 2, where m_1 is the mass of the payload, m_2 is the sum mass of the VCM mover, PZT, and connecting plate, k is the stiffness of the passive vibration isolation system, c is the damping of the passive vibration isolation system, f_v and f_p are the VCM force and PZT force, respectively, and x_1, x_2, and x_b are the displacements of the payload, VCM mover, and base, respectively.

2.2 Mathematical modeling of the DSA-SAVIS

The output force of the VCM follows Faraday's law:

$$f_v = NB\pi dI = k_i I, \tag{1}$$

where N is the number of coil turns, B is the average magnetic induction of the air gap, d is the diameter of the coil, I is the current value of the coil, and $k_i=NB\pi d$ is the thrust coefficient of the VCM.

The one-dimensional piezoelectric constitutive equation is as follows:

$$\begin{cases} D = d_{33}\sigma + \varepsilon_{33}E, \\ \sigma = E_p(\varepsilon - d_{33}E), \end{cases} \tag{2}$$

where D is the longitudinal electric displacement, d_{33} is the longitudinal piezoelectric strain coefficient, σ is the longitudinal stress of the piezoelectric ceramic piece, ε_{33} is the dielectric constant, E is the longitudinal electric field intensity, E_p is the elastic modulus of the PZT, and ε is the longitudinal strain.

The operating voltage, longitudinal displacement, and output force of the PZT actuator can be derived as

$$U = Eh, \tag{3}$$

$$\delta = n\varepsilon h, \tag{4}$$

$$f_p = -A\sigma = k_u U - k_p \delta, \tag{5}$$

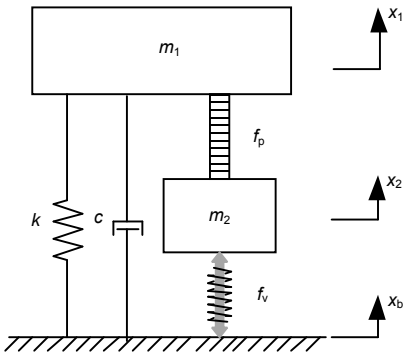

Fig. 2 Schematic of the designed DSA-SAVIS

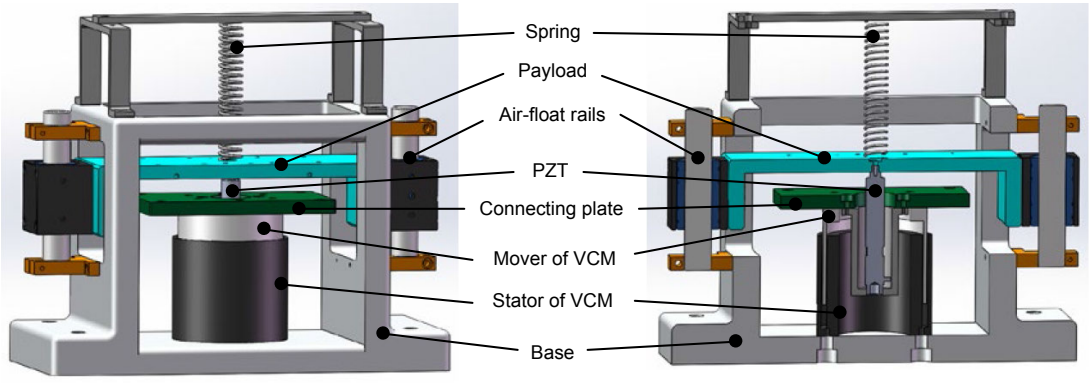

Fig. 1 Prototype of the designed dual-stage actuation semi-active vibration isolation system (DSA-SAVIS)

where h is the thickness of a single layer of the stacked actuator, n is the number of stacked ceramic layers, A is the area of the piezoelectric ceramic piece, $k_u=AE_pd_{33}/h$ is the force coefficient of the PZT, and $k_p=AE_p/(nh)$ is the stiffness of the PZT.

Because the stiffness of the piezoelectric ceramics is too large, it is reduced by connecting a PZT series with springs. The stiffness of the PZT actuator can be rewritten as

$$k_p=\left[AE_pk_L/(nh)\right]\Big/\left[AE_p/(nh)+k_L\right], \tag{6}$$

where k_L is the stiffness of the springs.

The equation of motion of the DSA-SAVIS is given by

$$\begin{cases} m_2\ddot{x}_2=f_v-f_p, \\ m_1\ddot{x}_1=f_p-k(x_1-x_b)-c(\dot{x}_1-\dot{x}_b). \end{cases} \tag{7}$$

Substituting Eqs. (1) and (5) into Eq. (7) and noting that $\delta=x_1-x_2$, the dynamic equation becomes

$$\begin{cases} m_2\ddot{x}_2=k_iI-k_uU+k_p(x_1-x_2), \\ m_1\ddot{x}_1=k_uU-k_p(x_1-x_2)-k(x_1-x_b)-c(\dot{x}_1-\dot{x}_b). \end{cases} \tag{8}$$

2.3 Characteristic analysis

DSA-SAVIS is a linear time-invariant system, and it is assumed that the initial condition of the system is zero. Let control inputs become zero, namely, I=0 and U=0. Then the Laplace transform of Eq. (8) can be written as

$$\begin{cases} m_2s^2X_2(s)=k_pX_1(s)-k_pX_2(s), \\ m_1s^2X_1(s)=(-cs-k_p-k)X_1(s)+k_pX_2(s)+(cs+k)X_b(s). \end{cases} \tag{9}$$

The transfer function from x_b to x_1 is used to evaluate the vibration isolation performance. The transfer function of the system without any controller can be derived from Eq. (9):

$$\frac{X_1(s)}{X_b(s)}=\frac{m_2cs^3+m_2ks^2+k_pcs+kk_p}{m_1m_2s^4+m_2cs^3+(m_1k_p+m_2k+m_2k_p)s^2+k_pcs+kk_p}. \tag{10}$$

Fig. 3 shows the conceptual Bode diagram of the system without any controller. There are two resonant frequencies, ω_1 and ω_2. The value of c is less than 0.1, and consider that c has little influence on the frequency transfer characteristics. To express clearly the frequency transfer characteristics of the SAVIS, Eq. (10) is equivalent to

$$\begin{aligned} \frac{X_1(s)}{X_b(s)}&=\frac{m_2ks^2+kk_p}{m_1m_2s^4+(m_1k_p+m_2k+m_2k_p)s^2+kk_p} \\ &=\frac{k}{m_1}\frac{s^2+\omega_3^2}{(s^2+\omega_1^2)(s^2+\omega_2^2)}, \end{aligned} \tag{11}$$

where $\omega_1\omega_2=\omega_3\sqrt{k/m_1}$, $\omega_1^2+\omega_2^2=k_p/m_2+k/m_1+k_p/m_1$, and $\omega_3=\sqrt{k_p/m_2}$.

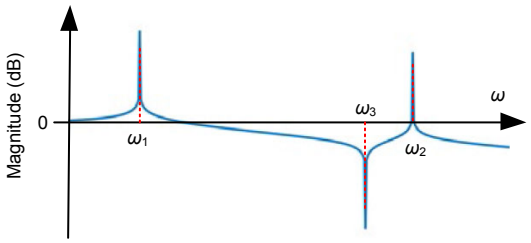

Fig. 3 Bode diagram of the system without any controller

When the frequency of the base vibration is around ω_1 or ω_2, the vibration is amplified. When the frequency of the base vibration equals ω_3, the ratio of x_1 to x_b subsequently becomes zero; the vibration is entirely isolated (Sun et al., 2003; Franček et al., 2019). The phenomenon is known as the anti-resonance, and therefore ω_3 is an anti-resonance frequency (Xu YF et al., 2015; Bai et al., 2019). The VCM mover, PZT, and connecting device can be considered a dynamic vibration absorber. It cleverly combines vibration isolation and vibration absorption technology, and has advantages of large static stiffness, suitability for low frequency vibration isolation, and high vibration isolation efficiency. Once the system is determined, the initial anti-resonance frequency is fixed. If the anti-resonance frequency can be adjusted to be equal to or close to the main frequency of the external disturbances in real time, DSA-SAVIS can achieve better vibration isolation performance.

3 Design and analysis of the controller

3.1 Design of the controller

According to Fig. 3, the design principle of the controller consists of two parts; one is to suppress the extra vibration whose frequency is around two resonant frequencies, ω_1 and ω_2 (Zuo and Slotine, 2005; Niu WC et al., 2018), whereas the other is to add a new anti-resonance frequency ω_4 which is adjustable by tracking the external disturbances in real time. Based on the above ideas, a closed-loop control block diagrammatic sketch is designed (Fig. 4).

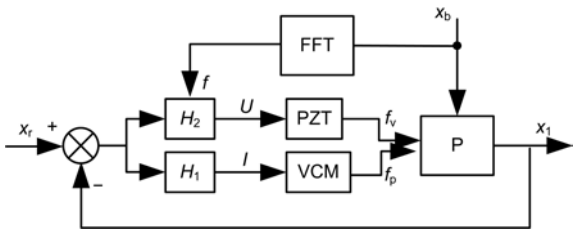

Fig. 4 Closed-loop control diagrammatic sketch

The difference between the expected value x_r and the actual one of the payload displacement x_1 is used as the input of the controller, and the outputs are the current value of the coil I and the voltage value of the PZT U. The main frequency of the base vibration f is obtained by fast Fourier transform (FFT), which is used as a reference to determine the newly added anti-resonance frequency ω_4. With the inputs of I and U, the driver produces a voice coil motor force f_v and the PZT stack force f_p to act on the payload. Above all, a closed-loop control is formed to isolate the base vibration.

The design of the controller contains two transfer functions from x_1 to I and from x_1 to U (Liu et al., 2018), namely, H_1 and H_2, respectively, which are designed as follows:

$$H_1(s)=\frac{I(s)}{X_1(s)}=K+\frac{1}{\tau s}, \tag{12}$$

$$H_2(s)=\frac{U(s)}{X_1(s)}=\frac{10^4}{s^2+\omega_4^2}, \tag{13}$$

where K is the adjustable proportional gain coefficient and τ is the adjustable integral gain coefficient.

By comparing the transmissibility curves of the simulation and experiment, it is verified that the system damping can be ignored (Song et al., 2018). From the Bode diagram, the attenuation amplitude of the transmissibility at the anti-resonance frequency point is −40 dB and −45 dB before and after the system damping is ignored, respectively. Then, the Laplace transform of Eq. (8) can be written as

$$\begin{cases} m_2 s^2 X_2(s)=k_i I(s)-k_u U(s)+k_p X_1(s)-k_p X_2(s), \\ m_1 s^2 X_1(s)=k_u U(s)-(k_p+k)X_1(s)+k_p X_2(s)+kX_b(s). \end{cases} \tag{14}$$

Substituting Eqs. (12) and (13) into Eq. (14) yields the expression of the transfer function of the system with the designed controller:

$$\frac{X_1(s)}{X_b(s)}=\frac{ks(s^2+\omega_3^2)(s^2+\omega_4^2)}{a_1 s^7+a_2 s^5+a_3 s^3+a_4 s^2+a_5 s+a_6}, \tag{15}$$

where ω_3 and ω_4 are the initial anti-resonance frequency and the added anti-resonance frequency as defined in Sections 2.3 and 3, respectively. a_1–a_6 are as follows:

$$\begin{cases} a_1=m_1 m_2, \\ a_2=m_1 k_p+m_2 k_p+m_2 k+m_1 m_2 \omega_4^2, \\ a_3=m_1 k_p \omega_4^2-10^4 m_2 k_u+m_2 k_p \omega_4^2-k_p k_i K+m_2 k \omega_4^2+k k_p, \\ a_4=-k_p k_i/\tau, \\ a_5=k k_p \omega_4^2-k_p k_i K \omega_4^2, \\ a_6=-k_p k_i \omega_4^2/\tau. \end{cases}$$

Fig. 5 shows the conceptual Bode diagram of the system with the designed controller. Compared with Fig. 4, the proposed controller suppresses the extra vibration whose frequency is around ω_1 or ω_2. Simultaneously, an adjustable anti-resonance frequency ω_4 is added to the closed-loop system Bode diagram so that the vibration can be isolated without energy consumption. The purpose of the proposed control method is to adjust the anti-resonance frequency according to the external disturbances and to make the best of the unique advantage of the dynamic vibration absorption.

3.2 Selection of parameters

The designed controller contains three parameters, K, τ, and ω_4. ω_4 is up to the main frequency of the base vibration to decide.

After the analysis by Lawes criterion, the constraint conditions of the system stability are written as

$$\begin{cases} K < (m_1 k_p + m_2 k_p + m_2 k)\omega_4^2 + k k_p - 10^4 m_2 k_u, \\ \tau > 0. \end{cases} \tag{16}$$

The optimum solutions of K and τ are as follows:

$$\min_{K,\tau} \quad G_{\min}$$
$$\text{s.t.} \begin{cases} K<(m_1 k_p+m_2 k_p+m_2 k)\omega_4^2 + k k_p - 10^4 m_2 k_u, \\ \tau > 0, \\ |I| < I_{\max}, \\ |U| < U_{\max}, \end{cases} \tag{17}$$

where $G_{\min}$ is the minimum value of the closed-loop gain, $I_{\max}$ is the maximum of the current value of the VCM, and $U_{\max}$ is the maximum of the voltage value of the PZT.

$G_{\min}$ can be derived as

$$G_{\min} = \inf\left(20\lg\left(\left|H(\mathrm{j}\omega)\right|\right)\right), \tag{18}$$

where

$$\left|H(\mathrm{j}\omega)\right| = \frac{k\omega(\omega_3^2-\omega^2)(\omega_4^2-\omega^2)}{\sqrt{(a_6-a_4\omega^2)^2+(-a_1\omega^7+a_2\omega^5-a_3\omega^3+a_5\omega)^2}}. \tag{19}$$

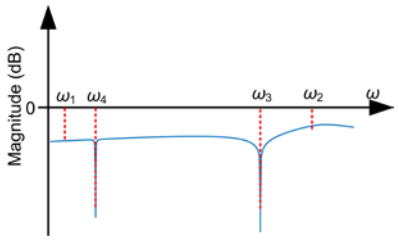

Fig. 5 Bode diagram of the system with the designed controller

Fig. 6 shows the relationship of $G_{\min}$, K, and τ. Initially, three different τ values are selected and set as 0.4×10^{-4}, 0.5×10^{-4}, and 0.6×10^{-4}. Therefore, three relationship curves of $G_{\min}$ with K are obtained when each τ is fixed (Fig. 6a). Similarly, three different K values are selected and set as 300, 600, and 900. Then, three relationship curves of $G_{\min}$ with τ are obtained when each K is fixed (Fig. 6b).

By comparing Figs. 6a and 6b, we can determine that with the decrease of K and τ, $G_{\min}$ decreases.

The transfer function from the velocity of the base vibration v_b to I can be written as

$$\frac{I(s)}{V_b(s)} = \frac{k(K\tau s+1)(s^2+\omega_3^2)(s^2+\omega_4^2)}{b_1 s^7 + b_2 s^5 + b_3 s^3 + b_4 s^2 + b_5 s + b_6}, \tag{20}$$

where $b_1=\tau a_1$, $b_2=\tau a_2$, $b_3=\tau a_3$, $b_4=\tau a_4$, $b_5=\tau a_5$, $b_6=\tau a_6$.

The maximum of the gain of v_b to I, i.e., $|G_I|_{\max}$, can be derived as

$$\left|G_I\right|_{\max} = \sup\left(\left|H_I(\mathrm{j}\omega)\right|\right), \tag{21}$$

where

$$\left|H_I(\mathrm{j}\omega)\right| = \frac{\left|k\omega(\omega_3^2-\omega^2)(\omega_4^2-\omega^2)\right|\sqrt{(K\tau\omega)^2+1}}{\sqrt{(b_6-b_4\omega^2)^2+(-b_1\omega^7+b_2\omega^5-b_3\omega^3+b_5\omega)^2}}. \tag{22}$$

Fig. 7 shows the relationship curve of $|G_I|_{\max}$ and τ, and $G_{I\max}$ is the saturation value of $|G_I|_{\max}$. Initially, three different K values are selected and set as 300, 600, and 900. Then, three relationship curves of $|G_I|_{\max}$ with τ are obtained when each K is fixed. The intersection point of each curve with the saturation $G_{I\max}$ is the desirable minimum value of τ under the

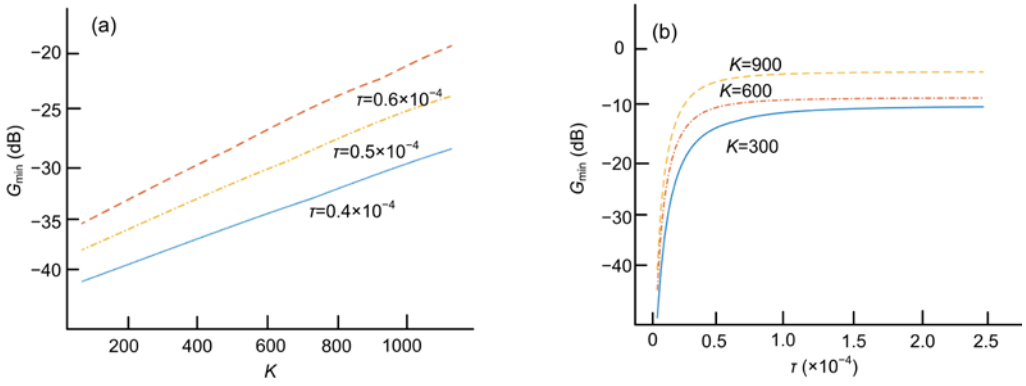

Fig. 6 Relationship curves of $G_{\min}$ and K (a) and $G_{\min}$ and τ (b)

corresponding K. From Fig. 7, we can determine that with the decrease of τ, $|G_I|_{\max}$ increases.

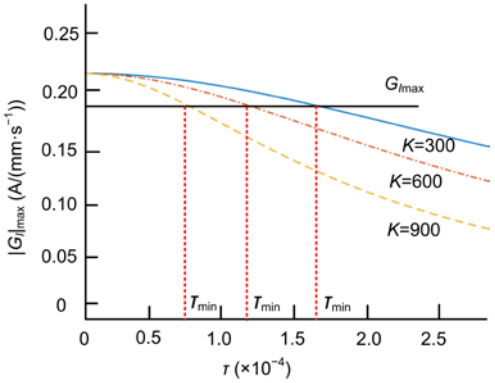

Fig. 7 Relationship curve of $|G_I|_{\max}$ and τ

Therefore, τ cannot be infinitely reduced due to the limitation of the range of the control signal I.

The transfer function from v_b to U can be written as

$$\frac{U(s)}{V_b(s)}=\frac{10^4 ks(s^2+\omega_3^2)}{a_1 s^7+a_2 s^5+a_3 s^3+a_4 s^2+a_5 s+a_6}. \quad (23)$$

The maximum of the gain of v_b to U, i.e., $|G_U|_{\max}$, can be derived as

$$\left|G_U\right|_{\max}=\sup\left(\left|H_U(\mathrm{j}\omega)\right|\right), \quad (24)$$

where

$$\left|H_U(\mathrm{j}\omega)\right|=\frac{10^4\left|k\omega(\omega_3^2-\omega^2)\right|}{\sqrt{(a_6-a_4\omega^2)^2+(-a_1\omega^7+a_2\omega^5-a_3\omega^3+a_5\omega)^2}}. \quad (25)$$

Fig. 8 shows the relationship curve of $|G_U|_{\max}$ and K, and $G_{U\max}$ is the saturation value of $|G_U|_{\max}$. Initially, three different τ values are selected and set as 0.4×10^{-4}, 0.5×10^{-4}, and 0.6×10^{-4}. Then three relationship curves of $|G_U|_{\max}$ with K are obtained when each τ is fixed. The relationship curves of $|G_U|_{\max}$ and K are the same under different values of τ, so the three curves coincide completely. The intersection point of each curve with the saturation $G_{U\max}$ is the desirable minimum value of K under the corresponding τ. From Fig. 8, we can determine that with the decrease of K, $|G_U|_{\max}$ increases.

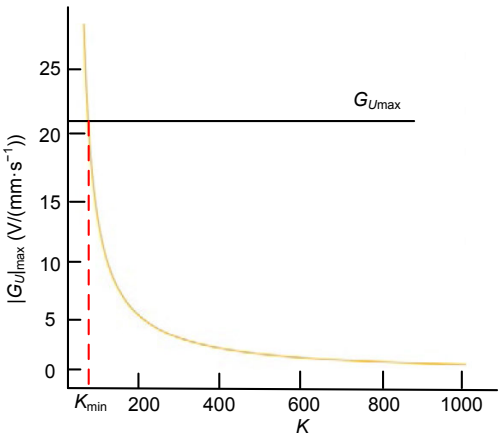

Fig. 8 Relationship curve of $|G_U|_{\max}$ and K

Therefore, K cannot be infinitely reduced due to the limitation of the range of the control signal U.

In this study, the permissible current control range of the VCM is −1.67–1.67 A, the permissible voltage control range of the PZT is 0–150 V, and the maximum speed of the base vibration is 7 mm/s. Based on the above analysis, the selection process of the parameters of the proposed controller is as follows: First, determine the anti-resonance frequency ω_4 to be added according to the main frequency of the base vibration. Then, based on Eq. (17) and the conclusions from Figs. 6–8, the optimum solutions of K and τ can be properly chosen for the designed controller for the best performance of the DSA-SAVIS.

4 Experiment verification

Fig. 9 shows the physical picture of the designed DSA-SAVIS whose parameters are listed in Table 1. Fig. 10 shows the experimental system. The absolute speeds of the base and the payload are measured by the GS-11D type piezoelectric vibration sensor (GS-11D, Geospace, USA). The GS-11D is a high-output, rotating coil geophone, designed and built to withstand shocks of rough handling. The precision springs of this field tested geophone are computer designed and matched to optimize performance specifications even under the most extreme conditions. The measuring signal is collected using a real-time target machine (NI PXIe-1062Q, National Instrument, USA). The controller is completed and then downloaded into the real-time target machine as well.

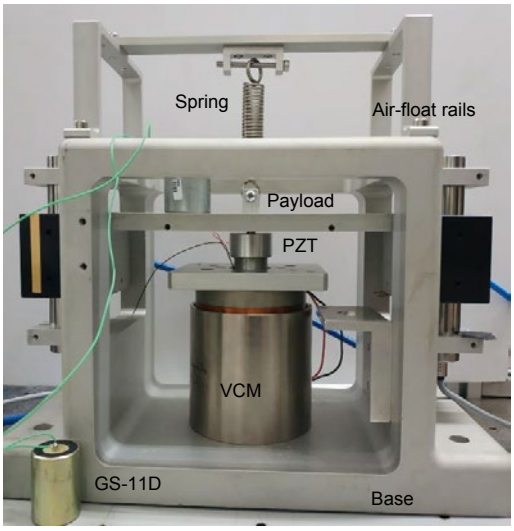

Fig. 9 Physical picture of the designed DSA-SAVIS

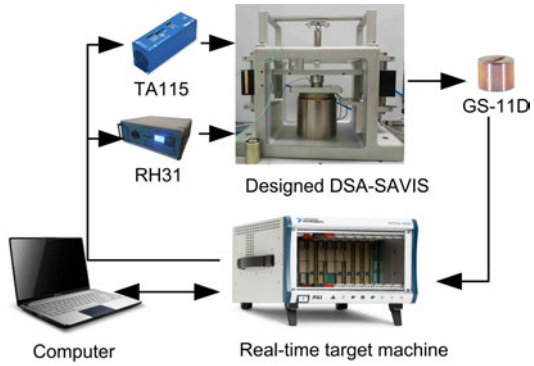

Fig. 10 Experimental system

Table 1 Parameters of the DSA-SAVIS

Parameter	Value
Mass of the payload, m_1 (kg)	0.695
Sum mass of the VCM mover, PZT, and the connecting plate, m_2 (kg)	0.614
Stiffiness of the passive vibration isolation system, k (N/m)	480
Stiffness of the PZT actuator, k_p (N/m)	5000
Thrust coefficient of the VCM, k_i (N/A)	31.8
Thrust coefficient of the PZT, k_u (N/V)	25.4

The control signal is calculated and then transferred to the drivers, the TA115 type power supply (TA115, Trustautomation, USA) of the voice coil motor and the RH31 type power supply (RH31, CoreMorrow, China) of the electromagnetic actuator. The supply voltage of TA115 is 24 to 48 V. The equivalent motor voltage can be increased up to ±43 V. The control signal voltage range of TA115 is 0–10 V and the gain is 0.2–0.8 A/V. In this experiment, we set the gain as 0.2 A/V. The control voltage range of RH31 (RH31, CoreMorrow, China) is 0–5 V and the gain is approximately 30.75 through experimental calibration. The VCM and PZT are driven for active vibration control.

4.1 Experiment verification of frequency domain

The external vibration is generated by hitting the base with a Japan pulse hammer (GK-2110, ONO-SOKKI, Japan), and is detected and analyzed by a 941B type vibration analyzer (941B, Boyuan Electronic Technology, China). The transmissibility of the DSA-SAVIS without any controller is measured (Fig. 11). The two resonance frequencies are approximately 8.8 and 17.5 Hz, and the anti-resonance frequency is approximately 14.3 Hz. Fig. 12 indicates that the resonance peaks are eliminated with the proposed controller. Furthermore, the transmissibility is less than −5 dB for the whole frequency band, less than −15 dB when the frequency is lower than the initial anti-resonance frequency, and less than −30 dB when the frequency is around the added anti-resonance frequency. With the change of the controller parameter, the added anti-resonance frequency of the system changes simultaneously. The experimental results are consistent with the theoretical one of the proposed controller.

4.2 Experiment verification of vibration isolation

The external vibration is generated by hitting the base with a GK-2110 Japan pulse hammer (GK-2110,

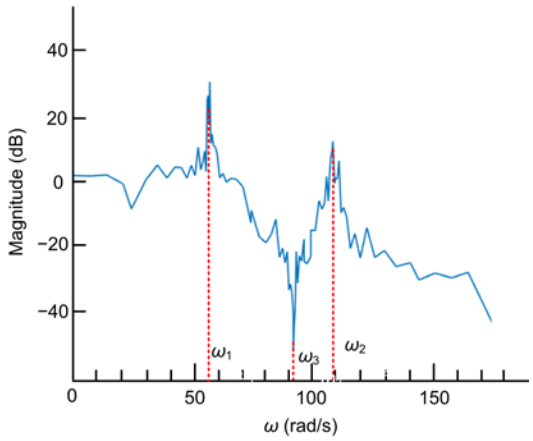

Fig. 11 Transmissibility curve of the DSA-SAVIS without any controller

ONOSOKKI, Japan). The velocities of the base and the payload are measured by the GS-11D type speed sensor (GS-11D, Geospace, USA). Based on the FFT results of the external vibration, ω_4=20, K=100, and τ=0.000 01 are set for the proposed controller.

Fig. 13b infers that the proposed controller achieves a good performance for isolating the external disturbances. Without any controller, the base vibration velocity is 6 mm/s, the maximum velocity of the payload vibration is 4 mm/s, the payload continues to oscillate, and the vibration attenuation is slow. With the proposed controller, the payload vibration velocity decays more rapidly, and the maximum velocity of the payload vibration is 0.5 mm/s with a reduction of 87.5% compared to that without the controller. Fig. 13c shows that when both the VCM and PZT work, the system can have a good vibration isolation effect on the external vibration. If only one of them works, the vibration isolation effect is not ideal. This indirectly indicates that VCM and PZT are indispensable in the design of a system controller.

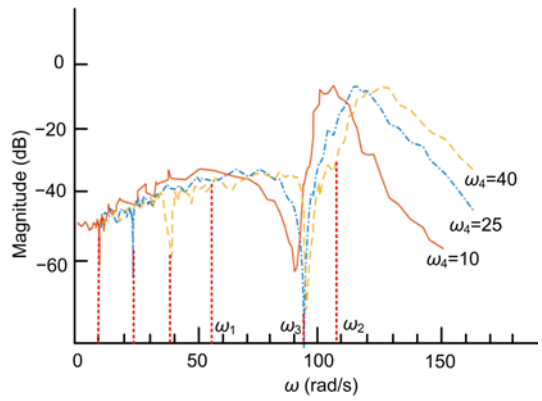

Fig. 12 Transmissibility curve with the designed controller

Fig. 14 shows that the peak frequency point of the spectrum is approximately 20 rad/s by the FFT of the base velocity, and the amplitude is 0.48 mm/s. With the proposed controller, the amplitude of the payload's velocity is 0.11 mm/s at 20 rad/s, with a reduction of 77.1%. The attenuation effect is better than those of other frequency points. This verifies the remarkable vibration isolation effect at the anti-resonance frequency point which is consistent with preset ω_4.

Fig. 15 shows the vibration isolation performance of the whole system when the platform base is applied with the frequency sweeping disturbances, which is generated by a vibration exciter. Set 5, 10, 15, 20, and 30 Hz as the sweeping frequencies, the amplitude of each frequency disturbance is set to the same, 5 mm/s, and each frequency disturbance continues 2.5 s. When the sweeping frequency of the disturbance changes, the controller will adjust the parameters in real time to realize the anti-resonance frequency point tracking. The results of FFT analysis

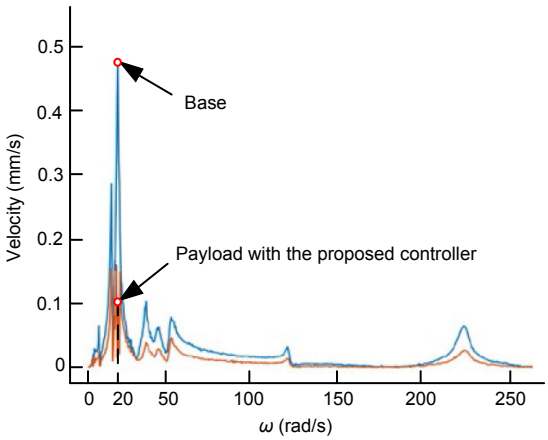

Fig. 14 Frequency spectrum of the base and the payload's velocity

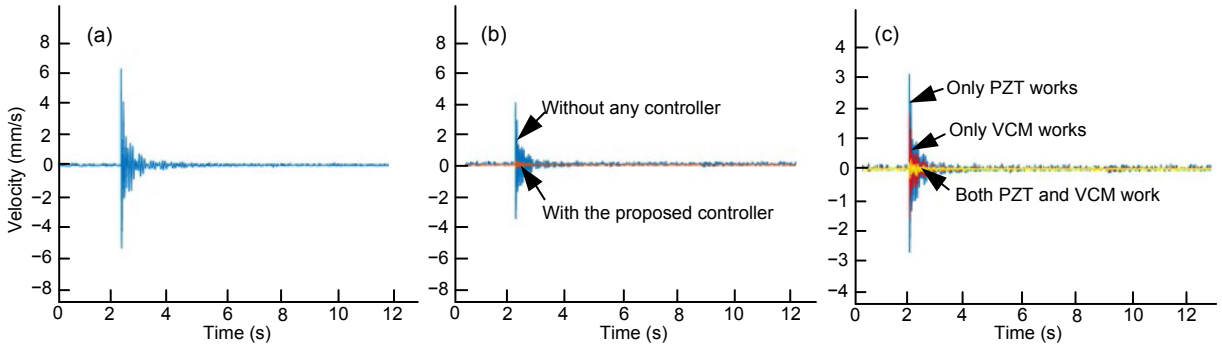

Fig. 13 Velocity of the base (a), velocity of the payload with and without controller (b), and velocity of the payload when only PZT works, only VCM works, and both the PZT and VCM work (c)

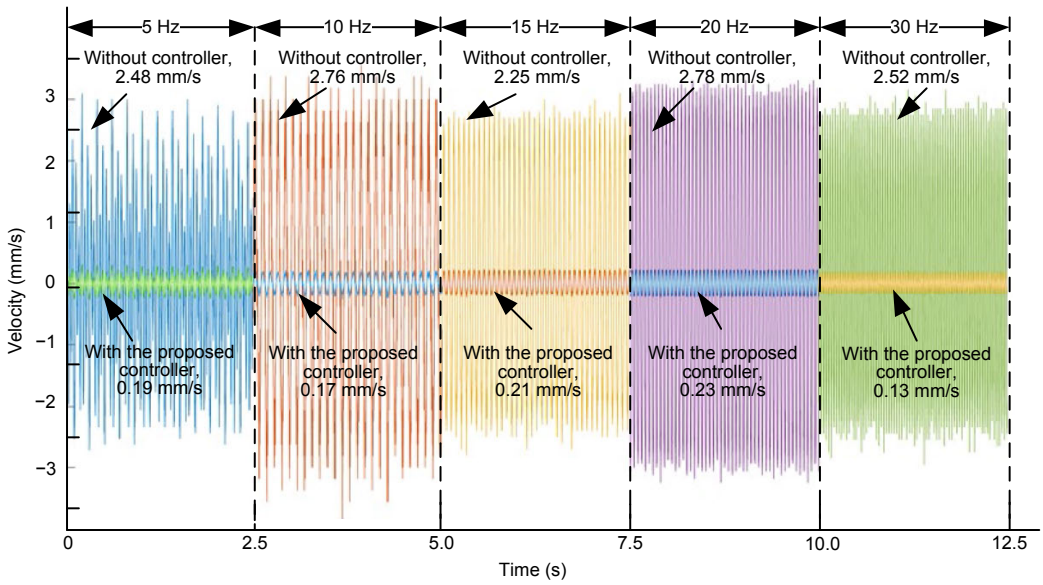

Fig. 15 Velocity of the payload with frequency sweeping disturbances

show that the transmissibility at 5, 10, 15, 20, and 30 Hz is −28.4, −29.4, −27.5, −26.7, and −25.7 dB, respectively, with a reduction of 92.3%, 93.8%, 90.7%, 91.7%, and 94.8%, respectively, compared with that without the controller.

The payload velocity is used as the input of the proposed controller, and the outputs are the current value of the coil I and the voltage value of the PZT U. Fig. 16 shows that following the principle of selecting parameters of the controller proposed in Section 3, the control signals I and U are not saturated, which is in accordance with the expected requirement of the experiment and verifies the design rationality of the previous controller.

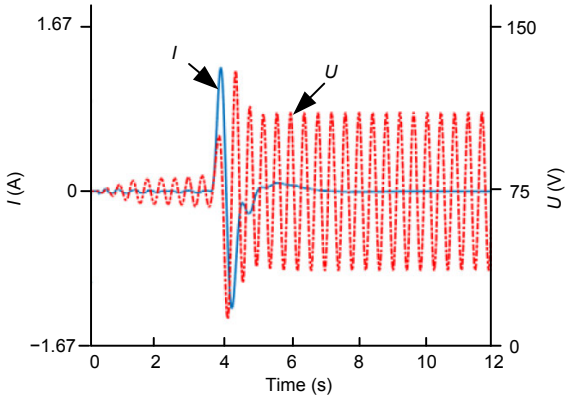

Fig. 16 Curves of the control signals *I* and *U*

5 Conclusions

Based on the unique dynamic vibration absorption characteristic of the DSA-SAVIS, an adjustable anti-resonance frequency controller is proposed. The dynamic vibration absorption point is adjusted in real time by tracking the external disturbances to achieve good vibration isolation performance. The proposed control method makes full use of the anti-resonance characteristic of dynamic vibration absorption. The experimental results showed that the closed-loop transmissibility is less than −5 dB in the whole frequency band. Without any controller, the operating frequency of the system ranges from 11.1 to 17.5 Hz and the corresponding bandwidth is 6.4 Hz. When the proposed controller is introduced, the bandwidth is extended to the full band. Furthermore, the closed-loop transmissibility is less than −30 dB around the added anti-resonance frequency, which can be adjusted from 0 Hz to the initial anti-resonance frequency. This is the best working frequency for the system to isolate the vibration effectively with the anti-resonance frequency we added. With the proposed controller, the disturbance amplitude of the payload decays from 4 to 0.5 mm/s with a reduction of 87.5% for the impulse disturbance applied to the platform base. Concurrently, the system can adjust anti-resonance frequency point in real time by tracking the frequency sweeping disturbances, and a good vibration isolation performance is achieved. The closed-

loop transmissibility at a different sweeping frequency is below −25.7 dB, and the reduction is above 90.7% compared with that without the controller. The whole system has characteristics of adjustable vibration absorption point, long stroke, high precision, and wide band. This indicates that the proposed control method has good application prospects in the guarantee of an ultra-low vibration environment, especially at the frequency sweeping in the semiconductor manufacturing industry.

Contributors

Bo ZHAO and Jiubin TAN designed the research. Weijia SHI and Bingquan WANG processed the data. Bo ZHAO drafted the manuscript. Weijia SHI and Bingquan WANG helped organize the manuscript. Jiubin TAN revised and finalized the paper.

Compliance with ethics guidelines

Bo ZHAO, Weijia SHI, Bingquan WANG, and Jiubin TAN declare that they have no conflict of interest.

References

Alujević N, Čakmak D, Wolf H, et al., 2018. Passive and active vibration isolation systems using inerter. *J Sound Vib*, 418:163-183. https://doi.org/10.1016/j.jsv.2017.12.031

Bai J, Daaoub A, Sangtarash S, et al., 2019. Anti-resonance features of destructive quantum interference in single-molecule thiophene junctions achieved by electrochemical gating. *Nat Mater*, 18(4):364-369. https://doi.org/10.1038/s41563-018-0265-4

Brennan MJ, 1997. Vibration control using a tunable vibration neutralizer. *Proc Inst Mech Eng C J Mech Eng Sci*, 211(2):91-108. https://doi.org/10.1243/0954406971521683

Bronowicki AJ, MacDonald R, Gursel Y, et al., 2003. Dual stage passive vibration isolation for optical interferometer missions. Proc SPIE 4852, Interferometry in Space, p.753-763. https://doi.org/10.1117/12.460731

Butler H, 2011. Position control in lithographic equipment. *IEEE Contr Syst Mag*, 31(5):28-47. https://doi.org/10.1109/MCS.2011.941882

Carre H, Doxtator RH, Duffy MC, 1982. Semiconductor manufacturing technology at IBM. *IBM J Res Dev*, 26(5): 528-531. https://doi.org/10.1147/rd.265.0528

Coronado A, Trindade MA, Sampaio R, 2013. Frequency-dependent viscoelastic models for passive vibration isolation systems. *Shock Vib*, 9(4-5):862159. https://doi.org/10.1155/2002/862159

Davis CL, Lesieutre GA, 2000. An actively tuned solid-state vibration absorber using capacitive shunting of piezoelectric stiffness. *J Sound Vib*, 232(3):601-617. https://doi.org/10.1006/jsvi.1999.2755

Ding D, Torres JA, Pan DZ, 2011. High performance lithography hotspot detection with successively refined pattern identifications and machine learning. *IEEE Trans Comput Aided Des Integr Circ Syst*, 30(11):1621-1634. https://doi.org/10.1109/TCAD.2011.2164537

Franček P, Petošić A, Budimir M, et al., 2019. Electrical resonance/antiresonance characterization of NDT transducer and possible optimization of impulse excitation signals width and their types. *NDT E Int*, 106:29-41. https://doi.org/10.1016/j.ndteint.2019.05.005

Ismagilov FR, Papini L, Vavilov VE, et al., 2020. Design and performance of a high-speed permanent magnet generator with amorphous alloy magnetic core for aerospace applications. *IEEE Trans Ind Electron*, 67(3):1750-1758. https://doi.org/10.1109/TIE.2019.2905806

Ito S, Neyer D, Pirker S, et al., 2015. Atomic force microscopy using voice coil actuators for vibration isolation. Proc IEEE Int Conf on Advanced Intelligent Mechatronics, p.470-475. https://doi.org/10.1109/AIM.2015.7222578

Ito S, Unger S, Schitter G, 2017. Vibration isolator carrying atomic force microscope's head. *Mechatronics*, 44:32-41. https://doi.org/10.1016/j.mechatronics.2017.04.008

Kamesh D, Pandiyan R, Ghosal A, 2012. Passive vibration isolation of reaction wheel disturbances using a low frequency flexible space platform. *J Sound Vib*, 331(6): 1310-1330. https://doi.org/10.1016/j.jsv.2011.10.033

Lee KW, Noh YJ, Arai Y, et al., 2011. Precision measurement of micro-lens profile by using a force-controlled diamond cutting tool on an ultra-precision lathe. *Int J Precis Technol*, 2(2-3):211-225. https://doi.org/10.1504/IJPTECH.2011.039460

Li D, Wang B, Tong Z, et al., 2019. On-machine surface measurement and applications for ultra-precision machining: a state-of-the-art review. *Int J Adv Manuf Technol*, 104(1-4):831-847. https://doi.org/10.1007/s00170-019-03977-8

Liu H, Cui SP, Liu YW, et al., 2018. Design and vibration suppression control of a modular elastic joint. *Sensors*, 18(6):1869. https://doi.org/10.3390/s18061869

Matichard F, Lantz B, Mittleman R, et al., 2015. Seismic isolation of advanced LIGO: review of strategy, instrumentation and performance. *Class Quantum Grav*, 32(18):185003. https://doi.org/10.1088/0264-9381/32/18/185003

Nagaya K, Kurusu A, Ikai S, et al., 1999. Vibration control of a structure by using a tunable absorber and an optimal vibration absorber under auto-tuning control. *J Sound Vib*, 228(4):773-792. https://doi.org/10.1006/jsvi.1999.2443

Nelson PG, 1991. An active vibration isolation system for inertial reference and precision measurement. *Rev Sci Instrum*, 62(9):2069-2075. https://doi.org/10.1063/1.1142368

Niu JC, Zhao GQ, Hu XX, 2005. Active control of structural vibration by piezoelectric stack actuators. *J Zhejiang Univ Sci*, 6(9):974-979. https://doi.org/10.1631/jzus.2005.A0974

Niu WC, Li B, Xin T, et al., 2018. Vibration active control of structure with parameter perturbation using fractional order positive position feedback controller. *J Sound Vib*, 430:101-114. https://doi.org/10.1016/j.jsv.2018.05.038

Qiu ZC, Wang XF, Zhang XM, et al., 2018. A novel vibration measurement and active control method for a hinged flexible two-connected piezoelectric plate. *Mech Syst Signal Process*, 107:357-395. https://doi.org/10.1016/j.ymssp.2018.01.037

Qu D, Liu XD, Liu GT, et al., 2019. Analysis of vibration isolation performance of parallel air spring system for precision equipment transportation. *Meas Contr*, 52(3-4): 291-302. https://doi.org/10.1177/0020294019836122

Song CS, Xiao Y, Yu CC, et al., 2018. H_∞ active control of frequency-varying disturbances in a main engine on the floating raft vibration isolation system. *J Low Freq Noise Vib Active Contr*, 37(2):199-215. https://doi.org/10.1177/1461348417725944

Sun T, Huang ZY, Chen DY, et al., 2003. Signal frequency based self-tuning fuzzy controller for semi-active suspension system. *J Zhejiang Univ Sci*, 4(4):426-432. https://doi.org/10.1631/jzus.2003.0426

Suzuki Y, Abe N, 2013. Variable stiffness system for semi-active vibration control by frequency. Proc Conf of Kanto Branch, p.923-928.

Wang H, Li B, Liu Y, et al., 2019. Low-frequency, broadband piezoelectric vibration energy harvester with folded trapezoidal beam. *Rev Sci Instrum*, 90(3):035001. https://doi.org/10.1063/1.5034495

Xu JW, Yang XF, Li W, et al., 2020. Research on semi-active vibration isolation system based on electromagnetic spring. *Mech Ind*, 21(1):101. https://doi.org/10.1051/meca/2019048

Xu YF, Liao H, Liu L, et al., 2015. Modeling and robust H-infinite control of a novel non-contact ultra-quiet Stewart spacecraft. *Acta Astronaut*, 107:274-289. https://doi.org/10.1016/j.actaastro.2014.11.033

Yang BB, Hu YF, Vicario F, et al., 2017. Improvements of magnetic suspension active vibration isolation for floating raft system. *Int J Appl Electromagn Mech*, 53(2):193-209. https://doi.org/10.3233/JAE-150167

Yin SH, Xu ZQ, Yu JW, 2012. The composite ultra-precision processing technology for the small aspheric mould of stainless steel. *Adv Mater Res*, 497:176-179. https://doi.org/10.4028/www.scientific.net/AMR.497.176

Yong C, Zimcik DG, Wickramasinghe VK, et al., 2004. Development of the smart spring for active vibration control of helicopter blades. *J Int Mat Syst Struct*, 15(1):37-47. https://doi.org/10.1177/1045389X04039655

Zhang F, Shao SB, Tian Z, et al., 2019. Active-passive hybrid vibration isolation with magnetic negative stiffness isolator based on Maxwell normal stress. *Mech Syst Signal Process*, 123:244-263. https://doi.org/10.1016/j.ymssp.2019.01.022

Zhao C, Chen DY, 2008. Semi-active fuzzy sliding mode control for floating raft isolation system. *Chin J Mech Eng*, 44(2):163-169 (in Chinese). https://doi.org/10.3321/j.issn:0577-6686.2008.02.028

Zuo L, Slotine JJE, 2005. Robust vibration isolation via frequency-shaped sliding control and modal decomposition. *J Sound Vib*, 285(4-5):1123-1149. https://doi.org/10.1016/j.jsv.2004.09.014